Electromagnetic Inverse Scattering from a Single Transmitter

Yizhe Cheng[1,*] Chunxun Tian[1,*] Haoru Wang[1] Wentao Zhu[2] Xiaoxuan Ma[1,3✉] Yizhou Wang[1]
[1] Center on Frontiers of Computing Studies, School of Computer Science, Peking University
[2] Institute of Digital Twin, Eastern Institute of Technology, Ningbo
[3] Robotics Institute, Carnegie Mellon University
[*]Equal contribution, random order. ✉ Corresponding author.

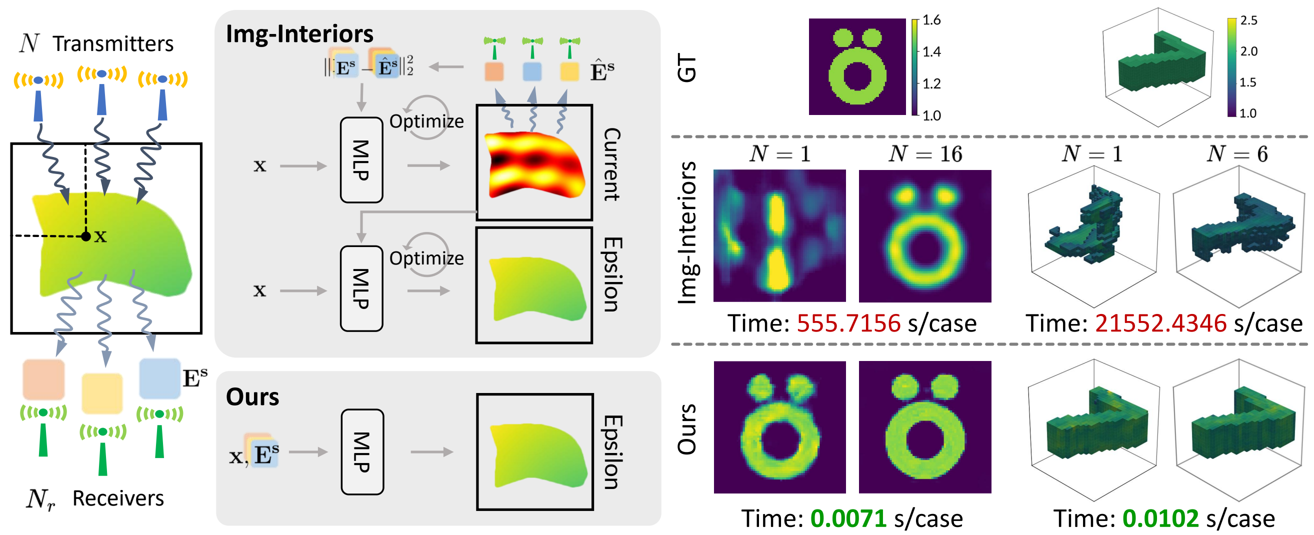

Figure 1. **Comparison between our method and the previous state-of-the-art. Left:** Img-Interiors [27] requires case-specific optimization to reconstruct the permittivity. In contrast, our method is a data-driven framework that operates in an *end-to-end*, *feed-forward* manner for solving inverse scattering. **Right:** Our method yields more accurate reconstructions than Img-Interiors [27]. It remains robust even with a *single* transmitter and achieves real-time inference with over $70,000\times$ speed-up.

Abstract

Electromagnetic Inverse Scattering Problems (EISP) seek to reconstruct relative permittivity from scattered fields and are fundamental to applications like medical imaging. This inverse process is inherently ill-posed and highly non-linear, making it particularly challenging, especially under sparse transmitter setups, e.g., *with only one transmitter. While recent machine learning-based approaches have shown promising results, they often rely on time-consuming, case-specific optimization and perform poorly under sparse transmitter setups. To address these limitations, we revisit EISP from a data-driven perspective. The scarcity of transmitters leads to an insufficient amount of measured data, which fails to capture adequate physical information for stable inversion. Accordingly, we propose a fully end-to-end and data-driven framework that predicts the relative permittivity of scatterers from measured fields, leveraging data distribution priors to compensate for the incomplete information from sparse measurements. This design enables data-driven training and feed-forward prediction of relative permittivity while maintaining strong robustness to transmitter sparsity. Extensive experiments show that our method outperforms state-of-the-art approaches in reconstruction accuracy and robustness. Notably, we demonstrate, for the first time, high-quality reconstruction from a single transmitter. This work advances practical electromagnetic imaging by providing a new, cost-effective paradigm to inverse scattering. Code and models are released at* https://gomenei.github.io/SingleTX-EISP/.

1. Introduction

Electromagnetic waves can penetrate object surfaces, making them essential for non-invasive imaging [17, 31]. At the core of electromagnetic imaging lies the Electromagnetic Inverse Scattering Problems (EISP), which seeks to reconstruct an object's relative permittivity from measured scattered electromagnetic field [29]. By solving EISP, we can accurately recover internal structures without physical intrusion [38], enabling a range of scientific and industrial applications, such as safer and more cost-effective alternatives to X-rays and MRI scans [5, 29, 31]. Typically, EISP necessitate a large number of transmitters and receivers to acquire sufficient measurement data. This requirement, however, leads to increased operational time and higher costs, thereby limiting the practical applicability of electromagnetic imaging techniques [22]. In contrast, reducing the number of transmitters offers significant advantages, including lower costs and easier deployment in constrained environments.[1, 3, 49]

However, the inherent ill-posed nature of EISP poses significant challenges to accurate reconstruction [7, 23, 27, 32, 42, 50–52, 56], particularly when only a limited number of transmitters are available. The scarcity of transmitters leads to an insufficient amount of measured data, which fails to capture adequate physical information for stable inversion. As a result, approaches relying solely on physical mechanisms[4, 6, 37, 55] often fail to achieve accurate reconstruction. Conventional numerical methods such as backpropagation (BP) [4], generally fail to produce reliable reconstructions under such limited-data conditions. Recent machine learning-based approaches like PGAN [39] and Physics-Net [26] often start with an initial solution derived from numerical methods, *i.e.*, BP, and frame the problem as an image-to-image translation task. With only a limited number of transmitters available, reliance on BP becomes a critical bottleneck. When BP fails, these methods are unable to correct its errors, as they are not fully end-to-end, ultimately leading to inaccurate reconstructions. The most recent method Img-Interiors [27] integrates physical mechanisms into neural networks and performs case-by-case optimization. However, in limited-transmitter scenarios, even after optimization has converged, the resulting reconstructions may still diverge substantially from the ground truth (Fig. 2), underscoring the intrinsic ambiguity of the inverse problem.

To address these limitations, we propose a *fully end-to-end* and *data-driven* framework that predicts the relative permittivity of scatterers from measured fields, leveraging data distribution priors to compensate for the scarcity of observational data. Unlike generative methods where data distribution priors typically refer to explicit, decoupled modules (e.g., denoisers modeling $p(x)$) [10, 21], our method learns an end-to-end mapping that implicitly leverages data statistics to resolve the inherent ill-posedness of electromagnetic inverse scattering problems. Specifically, our model takes the measured fields and the spatial coordinate of a position as input and directly predicts the relative permittivity at that location using Multilayer Perceptron (MLP)s, and is trained in a fully end-to-end manner against the ground-truth data. Our approach bypasses traditional numerical methods like BP, thereby avoiding the inherent constraints associated with conventional inversion techniques in limited-transmitter scenarios and fully exploiting the advantages of data-driven learning. This simple yet effective design enables efficient training across datasets and supports fast, feed-forward inference to achieve accurate and stable reconstruction predictions.

Extensive experiments demonstrate that our method outperforms existing State-of-the-Art (SOTA) methods on multiple benchmark datasets, especially under the challenging single-transmitter setting, where all previous methods fail (Fig. 5). It generalizes well to diverse scenarios and can be naturally extended to 3D scenes while maintaining high reconstruction accuracy. In summary, our contributions are threefold:

1) We systematically analyze the difficulty of lacking physical information faced by EISP in the setting of few transmitters, and point out that the missing information can be supplemented by data distribution priors.

2) Based on our analysis, we propose a *fully end-to-end* and *data-driven* model that does not rely on traditional numerical methods.

3) Extensive experiments show that our method outperforms existing SOTA approaches, especially under the challenging single-transmitter setting, marking a concrete step toward cost-effective and practical electromagnetic imaging solutions.

2. Related Work

2.1. Electromagnetic Inverse Scattering Problems

Solving EISP is to determine the relative permittivity of the scatterers based on the scattered field measured by the receivers, thereby obtaining internal imaging of the object. The primary challenges of EISP arise from its nonlinearity, ill-posedness, and errors introduced by the discretization [7, 23, 27, 32, 56]. Traditional methods for solving EISP can be categorized into non-iterative [4, 13, 18, 37] and iterative [6, 19, 41, 47, 55] approaches. Non-iterative methods, such as the Born approximation [37], the Rytov approximation [13, 18], and the BP method [4], solve nonlinear equations through linear approximations, which inevitably lead to poor quality of the results. For better reconstruction quality, iterative methods [6, 14, 19, 41, 47, 54, 55] such as 2-fold Subspace Optimization Method (SOM) [54] and Gs SOM [6] are proposed. To further overcome the ill-posedness of EISP, diverse regularization approaches and prior information have been widely applied [2, 25, 30, 36]. However, all of these methods are not generalizable and can be time-consuming because of the iterative schemes [26].

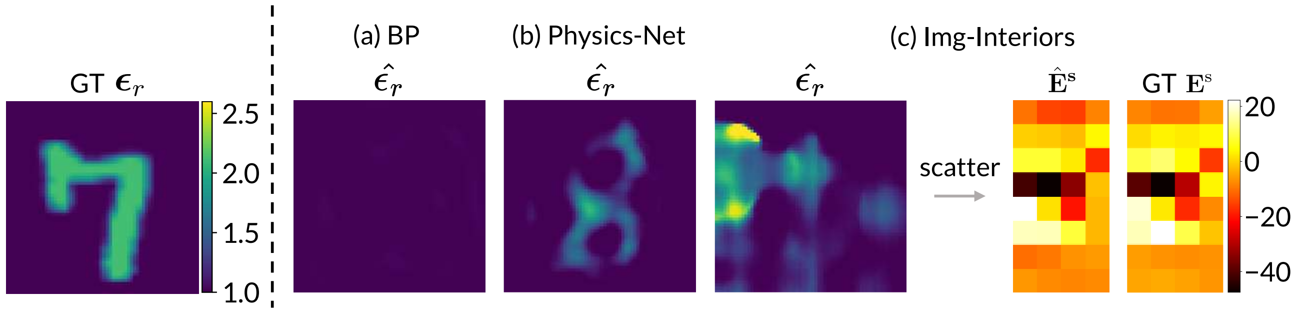

Figure 2. **Difficulties that previous methods faced under a single-transmitter setting.** (a) BP cannot reconstruct the scatterer. (b) Physics-Net makes incorrect guesses. (c) Although the reconstruction result of Img-Interiors is consistent with the measured field, the reconstructed scatterer itself is completely different from the ground truth.

2.2. Machine Learning for EISP

Recent studies shift to leveraging neural networks to solve this problem and demonstrate promising results [16, 24]. Some work [23, 26, 35, 39, 45, 48, 53] adopt a two-stage strategy: they use non-iterative methods such as BP [4] to generate initial estimates, which are then refined using image-to-image neural networks. While these approaches offer a degree of generalization, they are not end-to-end and remain dependent on BP initialization [4], which becomes their bottleneck. When physical data are too insufficient to reconstruct the scatterer, especially under single-transmitter settings, these approaches tend to "hallucinate" outputs according to unreliable initialization rather than predict the scatterer based on measured field (see Fig. 5). A more recent approach, Img-Interiors [27], integrates scattering mechanisms into the network architecture and achieves accurate reconstructions. However, it requires case-specific optimization, limiting generalization and making it vulnerable to local minima, often leading to failure in complex settings (see Figs. 4 and 7). Moreover, it fails under a single transmitter setting even when the optimization may have already converged because of ambiguity. While our method is also learning-based, it is an end-to-end feed-forward framework that simultaneously achieves generalization through data-driven learning. As a result, it consistently outperforms SOTA methods, particularly in the challenging single-transmitter setting where previous approaches fail.

3. Revisiting EISP

In this section, we revisit EISP and uncover its fundamental challenge: the inherent ill-posedness stemming from information scarcity.

Preliminary. In the forward process, the transmitters produce incident electromagnetic field $\mathbf{E}^{\text{i}}$ to the scatterer, generating scattered electromagnetic field $\mathbf{E}^{\text{s}}$. EISP is the inverse problem of the forward process. That is, for an unknown scatterer, we use transmitters to apply certain incident field $\mathbf{E}^{\text{i}}$ to it, and measure the scattered field $\mathbf{E}^{\text{s}}$ as our input via receivers. Our goal is to reconstruct the relative permittivity ϵ_r throughout the scatterer. For a detailed introduction of EISP, please refer to our supplementary material (Sec. B). Specifically, the incident field $\mathbf{E}^{\text{i}}$ excites the induced current $\mathbf{J}$. Using the method of moments [33], the total field $\mathbf{E}^{\text{t}}$ for a given transmitter can be expressed as [8]:

$$\mathbf{E}^{\text{t}} = \mathbf{E}^{\text{i}} + \mathbf{G}^{\text{d}} \cdot \mathbf{J}, \tag{1}$$

where $\mathbf{E}^{\text{t}}$ is a vector of length M^2, and $\mathbf{G}^{\text{d}}$ is a constant $M^2 \times M^2$ matrix representing the discrete free-space Green's function in $\mathcal{D}$. The induced current field $\mathbf{J}$ satisfies:

$$\mathbf{J} = \text{Diag}(\boldsymbol{\xi}) \cdot \mathbf{E}^{\text{t}}, \tag{2}$$

where $\boldsymbol{\xi} = \boldsymbol{\epsilon}_r - 1$, $\text{Diag}(\boldsymbol{\xi})$ represents a diagonal matrix whose leading diagonal consists of $\boldsymbol{\xi}$. Then $\mathbf{J}$ serves as a new source to emit $\mathbf{E}^{\text{s}}$. For N_r receivers, the scattered field $\mathbf{E}^{\text{s}}$ can be got through $\mathbf{E}^{\text{s}} = \mathbf{G}^{\text{s}} \cdot \mathbf{J}$, where $\mathbf{G}^{\text{s}}$ is a constant $N_r \times M^2$ matrix representing the discrete Green's function. Since $N_r \ll M^2$ in practice, reconstructing the induced current $\mathbf{J}$ from the scattered field $\mathbf{E}^{\text{s}}$ is ill-posed.

Reduction of measured data. EISP is fundamentally challenged by nonlinearity and ill-posedness, especially when the amount of measured data is significantly reduced, such as under single-transmitter settings. We divide previous work into three categories and systematically analyze the difficulties they faced under this setting. (a) Conventional numerical approaches, such as BP [4], employ linear approximations, which limit their reconstruction quality. As shown in Fig. 2, BP cannot even reconstruct a rough shape of the scatterer. (b) Machine learning methods based on conventional numerical approaches [26, 39], such as Physics-Net. Although Physics-Net can leverage data-driven training to compensate for missing physical information, its strong dependency on BP initialization becomes a critical bottleneck. When BP fails, the model cannot correct the error of BP because it is not fully end-to-end, resulting inaccurate reconstructions, as shown in Fig. 2. (c) Machine learning methods based on implicit functions, such as Img-Interiors [27]. Img-Interiors reconstructs a scatterer through case-by-case optimization. As shown in Fig. 2, we use the scatterer reconstructed by Img-Interiors to simulate the scattered field, and the result closely matches the measured field. However, the scatterer

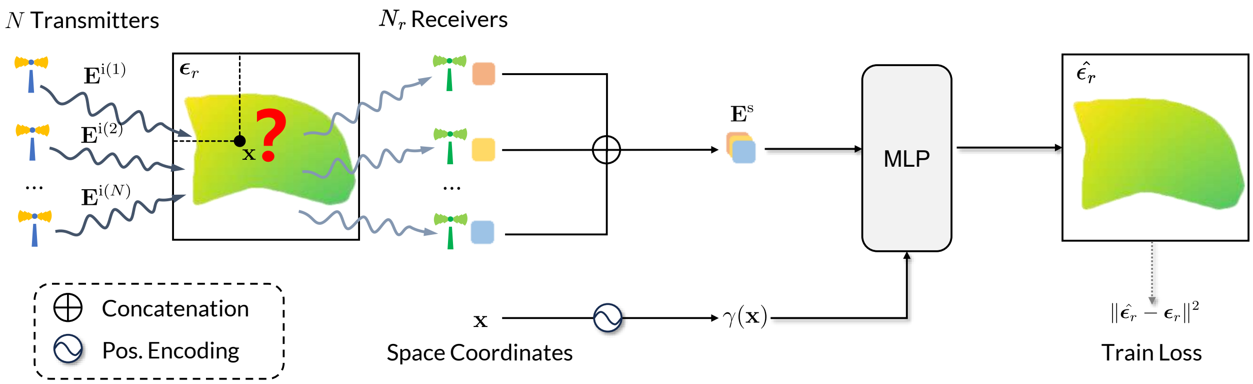

Figure 3. **Overview of our method.** Our pipeline is built around a MLP that serves as the inverse solver. Given the scattered field measurements $\mathbf{E}^{\mathrm{s}}$ from all transmitters and receivers, along with a spatial query $\mathbf{x}$, the MLP directly predicts the relative permittivity $\hat{\epsilon_r}(\mathbf{x})$. To enhance spatial expressiveness, we apply positional encoding $\gamma(\mathbf{x})$ to the query position. During training, dashed lines indicate the supervision signals applied.

itself deviates significantly from the ground truth, which shows the intrinsic ambiguity of the inverse problem. The core conclusion is that the severe information deficit makes a direct solution to the inverse problem fundamentally intractable. Consequently, any such attempt is bound to be fragile, highlighting the need for an alternative paradigm.

4. Method

4.1. Overview

To address the aforementioned limitations, we introduce our end-to-end, data-driven framework for EISP, as illustrated in Fig. 3. Our method employs an MLP that takes space coordinates $\mathbf{x}$ and corresponding scattered field measurements $\mathbf{E}^{\mathrm{s}}$ as input, and directly outputs the relative permittivity $\boldsymbol{\epsilon}_r$ at the specified locations. This approach effectively learns the mapping between scattered field $\mathbf{E}^{\mathrm{s}}$ and relative permittivity $\boldsymbol{\epsilon}_r$ through training on diverse scattering scenarios, thereby incorporating essential data distribution priors to compensate for the lack of physical information caused by insufficient measurements. In the following, we detail our model architecture (Sec. 4.2), and the training losses (Sec. 4.3).

4.2. Model Architecture

Based on the forward formulation of EISP in Sec. 3, where the scattered field measurements serve as input and the relative permittivity distribution represents the output, we design an end-to-end learning framework that directly learns this complex nonlinear mapping. As illustrated in Fig. 3, our approach employs an MLP that approximates the inverse mapping from spatial coordinates and scattered field data to the relative permittivity values, formulated as:

$$\hat{\epsilon_r}(\mathbf{x}_{\mathrm{i}}) = F_\theta(\mathbf{E}^{\mathrm{s}}, \gamma(\mathbf{x}_{\mathrm{i}})), \mathbf{x}_{\mathrm{i}} \in \mathbb{R}^2, \tag{3}$$

where $\mathbf{x}_{\mathrm{i}}$ represents the spatial coordinate, $\mathbf{E}^{\mathrm{s}}$ denotes the scattered field measured by all receivers, $F_\theta(\cdot)$ is an MLP with trainable parameters, and $\hat{\epsilon_r}(\mathbf{x}_{\mathrm{i}})$ is the predicted relative permittivity at the corresponding position. Recall that in Sec. 3, for a single transmitter, the scattered field $\mathbf{E}^{\mathrm{s}}$ is discretized as a real-valued vector of dimension $2N_r$, containing the real and imaginary parts of the measurements from all N_r receivers. In the multiple transmitter configuration, $\mathbf{E}^{\mathrm{s}}$ is constructed by combining the complex measurement data from all N transmitters, resulting in a real-valued vector of dimension $2N \cdot N_r$ that represents the wave propagation and scattering behavior under diverse illumination conditions provided by transmitters at different locations. To enhance the model's capacity to represent high-frequency features, we apply positional encoding to the spatial coordinates $\mathbf{x}_{\mathrm{i}}$, mapping them into a higher-dimensional Fourier feature space using the encoding function: $\gamma(x) = [\sin(x), \cos(x), \ldots, \sin(2^{\Omega-1}x), \cos(2^{\Omega-1}x)]$, where the hyperparameter Ω controls the spectral bandwidth. The complete relative permittivity distribution $\hat{\epsilon_r}$ is reconstructed by sampling the MLP at all grid points $\{\mathbf{x}_{\mathrm{i}}\}_{\mathrm{i}=1}^{M^2}$: $\hat{\epsilon_r} = \{F_\theta(\mathbf{E}^{\mathrm{s}}, \gamma(\mathbf{x}_{\mathrm{i}}))\}_{\mathrm{i}=1}^{M^2}$.

4.3. Training

Our training objective is defined by a single loss function designed to directly supervise the reconstruction accuracy of the relative permittivity distribution. The loss is formulated as: $\mathcal{L} = \|\hat{\epsilon_r} - \boldsymbol{\epsilon}_r\|^2$. where $\hat{\epsilon_r}$ denotes the predicted relative permittivity and $\boldsymbol{\epsilon}_r$ represents the ground truth. By minimizing this Mean Squared Error (MSE) loss between the predicted and true permittivity values, the model learns to infer the material properties directly from the scattered field measurements, effectively leveraging the data distribution priors to overcome the ill-posedness of the inverse problem. This simplified loss function ensures stable and efficient training.

Table 1. **Quantitative comparison results with SOTA methods.** For Circular-cylinder dataset (Circular) and MNIST dataset (MNIST) datasets, we report results under two noise levels: 5% and 30%. The best results are shown in **bold**, and the second-best results are underlined.

Method	MNIST (5%)			MNIST (30%)			Circular (5%)			Circular (30%)			IF		
	MSE ↓	SSIM ↑	PSNR ↑	MSE ↓	SSIM ↑	PSNR ↑	MSE ↓	SSIM ↑	PSNR ↑	MSE ↓	SSIM ↑	PSNR ↑	MSE ↓	SSIM ↑	PSNR ↑
Number of Transmitters: $N = 16$													$N = 8/18$		
BP [4]	0.177	0.719	16.43	0.178	0.716	16.38	0.052	0.905	27.41	0.053	0.904	27.42	0.190	0.779	16.19
2-fold SOM [54]	0.154	0.757	20.93	0.156	0.738	20.84	0.031	0.917	32.23	0.038	0.889	30.63	-	-	-
Gs SOM [6]	0.072	0.923	28.31	0.081	0.901	27.13	0.023	0.946	35.40	**0.024**	0.937	34.89	0.184	0.790	17.00
BPS [7, 45]	0.093	0.909	25.00	0.105	0.891	23.90	0.027	0.963	33.00	0.029	**0.956**	32.42	0.310	0.664	17.05
PGAN [39]	0.084	0.916	25.80	0.091	0.910	25.31	0.026	**0.966**	35.56	0.032	0.947	33.91	0.121	**0.926**	24.78
Physics-Net [26]	0.075	0.932	26.17	0.093	0.906	24.58	0.027	0.934	32.72	0.030	0.927	32.08	0.170	0.788	18.48
Two-Step [50]	0.111	0.835	23.17	0.111	0.835	22.91	0.059	0.830	25.92	0.091	0.848	23.94	-	-	-
Img-Interiors [27]	0.200	0.863	26.41	0.336	0.760	19.01	0.036	0.947	35.05	0.047	0.932	32.62	0.153	0.837	23.26
Ours	**0.039**	**0.978**	**32.11**	**0.050**	**0.966**	**29.91**	**0.020**	0.965	**36.92**	**0.024**	0.954	**35.19**	**0.094**	0.916	**24.89**
Number of Transmitters: $N = 1$															
BP [4]	0.194	0.698	15.40	0.194	0.696	15.40	0.065	0.892	25.30	0.065	0.892	25.30	0.199	0.770	16.29
2-fold SOM [54]	0.432	0.556	12.49	0.828	0.382	9.45	0.060	0.859	26.63	0.157	0.639	20.07	-	-	-
Gs SOM [6]	0.460	0.598	15.31	0.404	0.557	14.91	0.046	0.888	29.62	0.051	0.862	28.77	0.192	0.779	16.66
BPS [7, 45]	0.189	0.774	18.75	0.205	0.744	17.97	0.045	0.891	29.29	0.055	0.862	27.68	0.348	0.669	16.18
PGAN [39]	0.133	0.867	21.69	0.153	0.830	20.41	0.033	**0.932**	32.02	0.040	**0.914**	29.94	0.248	0.680	16.85
PhysicsNet [26]	0.137	0.798	19.98	0.152	0.783	19.38	0.055	0.887	26.60	0.056	0.890	26.48	0.175	0.771	17.45
Two-Step [50]	0.117	0.845	23.34	0.203	0.656	17.62	0.145	0.673	19.45	0.174	0.652	18.41	-	-	-
Img-Interiors [27]	0.305	0.604	16.06	0.467	0.484	12.47	0.096	0.855	26.19	0.153	0.806	20.90	0.305	0.705	17.34
Ours	**0.085**	**0.921**	**26.09**	**0.127**	**0.862**	**22.56**	**0.031**	0.931	**33.18**	**0.038**	**0.914**	**31.38**	**0.128**	**0.908**	**24.19**

5. Experiments

5.1. Setup

Datasets. We train and test our method on standard benchmarks used for EISP following previous work [26, 39, 45]. Datasets that share identical transmitter and receiver configurations are combined into a unified training set. 1) Synthetic Circular [27] is synthetically generated comprising images of cylinders with random relative radius, number, location, and permittivity. 2) Synthetic MNIST [12] contains grayscale images of handwritten digits. For the two synthetic datasets, following previous work[12, 27], we evaluate two levels of noise: 5% and 30%, and the number of receivers $N_r = 32$. 3) Real-world Institut Fresnel's database (IF) [15] contains three different dielectric scenarios, namely FoamDielExt, FoamDielInt, and FoamTwinDiel, where $N_r = 241$. 4) Synthetic 3D MNIST dataset (3D MNIST) [11] contains 3D data of handwritten digits. 5) 3D ShapeNet dataset (3D ShapeNet) [46] contains 3D data of various shapes. $N_r = 160$ for the two 3D datasets. For more details about datasets, please refer to Sec. C.

Baselines and Metrics. For a fair comparison, we follow the same setting as in previous work [35, 39, 45] using their official code and train or optimize each method under the same setup as ours [1]. Specifically, we compare our method with 3 traditional methods and 4 deep learning-based approaches: 1) **BP** [4]: A traditional non-iterative inversion algorithm. 2) **2-fold SOM** [54]: A traditional iterative minimization scheme by using SVD decomposition. 3) **Gs SOM** [6]: A traditional subspace-based optimization method by decomposing the operator of Green's function. 4) **BPS** [7, 45]: A CNN-based image translation method with an initial guess from the BP algorithm. 5) **Physics-Net** [26]: A CNN-based approach that incorporates physical phenomena during training. 6) **Two-Step** [50]: A CNN-based approach with two steps. 7) **PGAN** [39]: A CNN-based approach using a generative adversarial network. 8) **Img-Interiors** [27]: An implicit approach optimized by forward calculation. Following previous work [26], we evaluate the quantitative performance of our method using PSNR [43], SSIM [44], and Relative Root-Mean-Square Error (MSE) [39].

5.2. Comparison with SOTAs

5.2.1. Multiple Transmitter Evaluation

We begin by comparing our method against prior approaches under the multiple-transmitter setting, using both synthetic and real datasets for comprehensive evaluation. As shown in the upper part of Tab. 1, our method achieves comparable

[1] BPS, Physics-Net, PGAN and Two-Step are trained as they are learning-based methods; all other baselines are optimization-based; we train separate models for each noise level for both our method and other learning-based models.

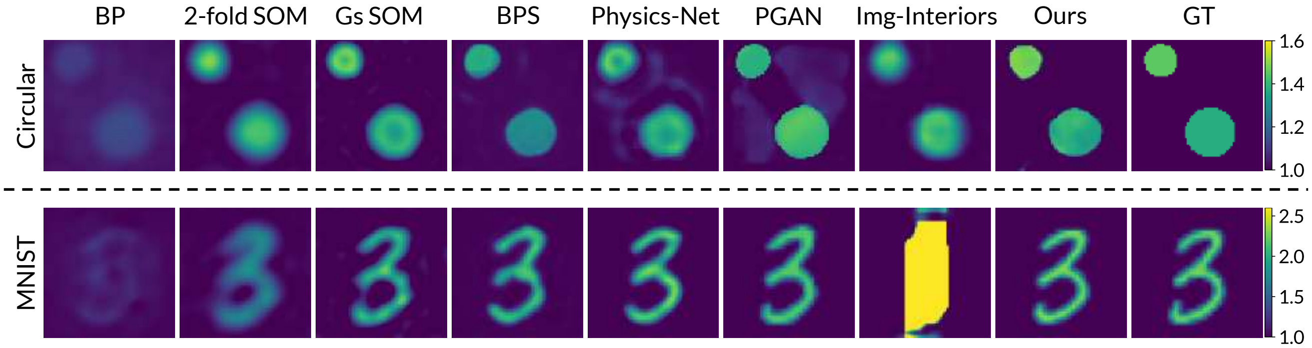

Figure 4. **Qualitative comparison under the multiple-transmitter setting.** The results are obtained with $N = 16$ transmitters and a noise level of 5%. Colors represent the values of the relative permittivity.

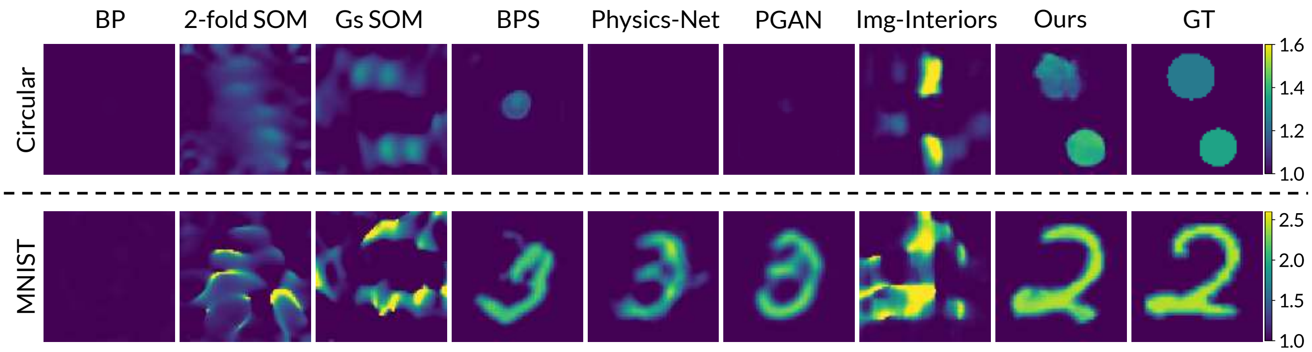

Figure 5. **Qualitative comparison under the single-transmitter setting.** Results are obtained with $N = 1$ transmitter and noise level of 5%. Colors represent the values of the relative permittivity.

or superior performance to the SOTA in most cases, demonstrating how our end-to-end training framework successfully leverage the data prior across diverse data domains. In addition, we present a qualitative comparison, as shown in Fig. 4. Traditional methods such as BP[4], Gs SOM [6], and 2-fold SOM [6] are only capable of recovering the coarse shape of the scatterer. BPS [7, 45] produces sharp edges, but the reconstructed shapes are often inaccurate. PGAN [39] achieves accurate shape recovery, yet introduces noticeable background artifacts. Img-Interiors [27] can generate high-quality reconstructions, but occasionally fails due to local optima, as it is based on an iterative optimization process (see the last row). In contrast, our method produces accurate and clean reconstructions across all cases, demonstrating both visual fidelity and robustness.

5.2.2. Single Transmitter Evaluation

Furthermore, we investigate a highly challenging and practically important setting that has been largely underexplored in previous work: performing EISP with a minimal number of transmitters. Specifically, we consider the most extreme case, using only a single transmitter. As shown in the lower part of Tab. 1, our method significantly outperforms all previous approaches across all datasets and noise levels. This remarkable performance under such constrained conditions underscores the efficacy of our end-to-end training framework, which successfully encodes and leverages rich data priors to achieve state-of-the-art results across diverse domains. To better understand this phenomenon, we present qualitative comparisons in Fig. 5 for synthetic data and Fig. 6 for real-world IF [15]. Traditional methods such as BP[4], Gs SOM [6], and 2-fold SOM [6] produce only blurry reconstructions. Deep learning-based methods like BPS [7, 45], Physics-Net [26], and PGAN [39] tend to "hallucinate" the digit, resulting in wrong shape on the MNIST dataset. Img-Interiors [27] fails to capture the fundamental morphology of the scatterer, resulting in structurally inaccurate representations that deviate significantly from the ground truth. Among all the methods, only ours can still produce reasonably accurate reconstructions of the relative permittivity under such an extreme condition.

5.3. Ablation Study

Noise Robustness. To simulate real-world sensor noise and related perturbations, we evaluate the robustness of the models by adding noise to the scattered field. Moving beyond simple binary testing, we systematically assess the model's performance across multiple noise levels ranging from 5% to 30% to examine its behavior in various noisy environments. The quantitative results presented in Tab. 2 demonstrate that

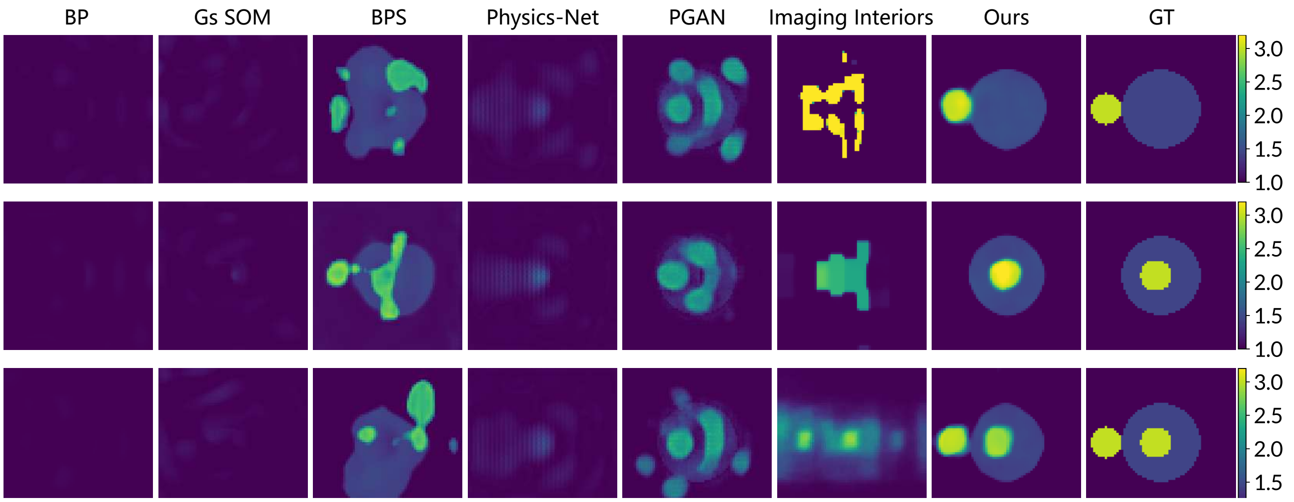

Figure 6. **Qualitative comparison under single-transmitter setting on real-world IF dataset.** The results are obtained with $N = 1$ transmitter, without noise level. Colors represent the values of the relative permittivity.

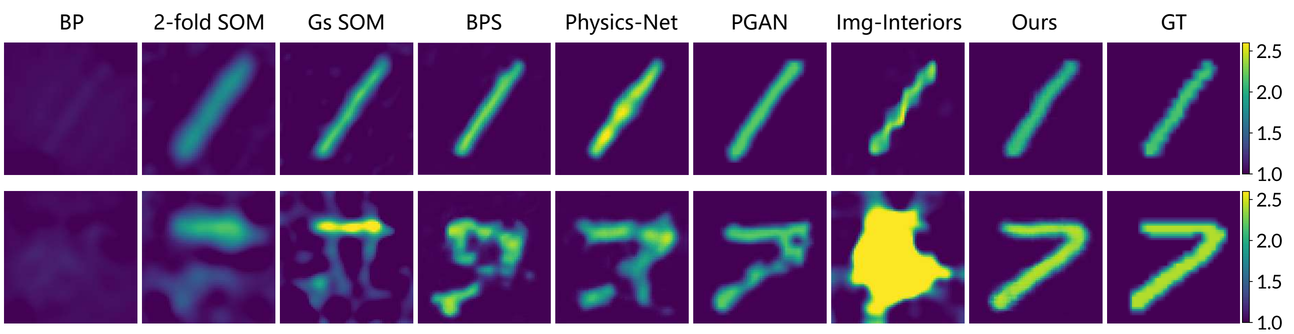

Figure 7. **Qualitative comparison under high noise setting.** The results are obtained with $N = 16$ transmitters and a noise level of 30%. Colors represent the values of the relative permittivity.

our model exhibits smooth and gradual performance degradation as the noise level increases, maintaining excellent reconstruction capability even under strong noise interference as high as 30%. Qualitative visualizations in Fig. 7 show that most baseline methods exhibit noticeable artifacts or even complete failure under severe noise conditions, while our method remains robust and preserves the essential structure of the target.

Ablation on Training Data Size. To investigate the dependency of model performance on training data volume, we trained our model on varying scales of data from 100% down to 25% and evaluated them on a complete test set. The quantitative results are presented in Tab. 3. First, our model demonstrates remarkable data efficiency, maintaining strong performance even when trained on partial datasets. Second, the performance degradation becomes substantially more pronounced under high-noise conditions. The performance penalty for data reduction is markedly severer in high-noise scenarios. This pronounced contrast underscores that sufficient training data is crucial for the model to learn robust features capable of countering strong noise interference.

5.4. Reconstruction on 3D data

Setup and Metrics. Our method can be naturally extended to 3D scenarios. We use the same MLP architecture, with the input dimension extended to 3. Following previous work [27], we employ the Synthetic 3D MNIST [11] and extend to 3D ShapeNet [46] for training and testing. For evaluation, we adopt 3D versions of the MSE [39] and Intersection over Union (IoU) as our metrics. Further details on the datasets are provided in Sec. C.

Results. We evaluate our method and Img-Interiors under limited-transmitter settings. Quantitative results demonstrate the superiority of our approach: on 3D MNIST, our method achieves an MSE of 0.120 and IoU of 0.769 with $N = 1$ transmitter, significantly outperforming Img-Interiors which obtains an MSE of 0.372 and IoU of 0.094 under the same conditions. With $N = 6$ transmitters, our results further improve to MSE of 0.094 and IoU of 0.834. For the more complex 3D ShapeNet dataset under $N = 1$ configuration, our method obtains an MSE of 0.064 and IoU of 0.762, showcasing its generalization capability to diverse 3D structures.

Table 2. **Ablation study of noise levels effects on MNIST under the multiple-transmitter setting.**

Noise Level	MSE ↓	SSIM↑	PSNR↑
5%	0.039	0.978	32.11
10%	0.039	0.978	32.18
15%	0.043	0.973	31.30
20%	0.043	0.974	31.34
25%	0.046	0.970	30.59
30%	0.050	0.966	29.91

Table 3. **Ablation study on training data size under the mutiple-transmitter setting.** Noise levels (5% and 30%) in parentheses.

Data	MNIST (5%)			MNIST (30%)		
	MSE ↓	SSIM↑	PSNR↑	MSE ↓	SSIM↑	PSNR↑
100%	0.039	0.978	32.11	0.050	0.966	29.91
75%	0.043	0.974	31.63	0.059	0.956	28.77
50%	0.048	0.968	30.68	0.068	0.944	27.69
25%	0.064	0.948	28.89	0.101	0.902	25.44

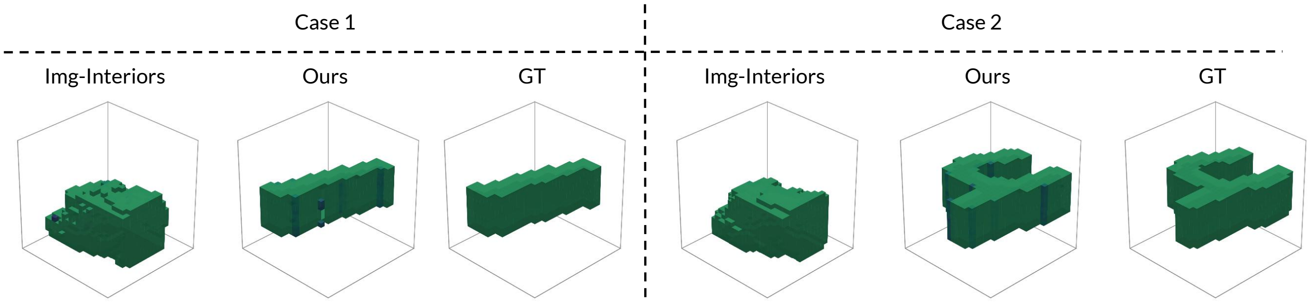

Figure 8. **Qualitative comparison under the single-transmitter setting for 3D reconstruction on 3D MNIST dataset.** The results are obtained with a single transmitter ($N = 1$). The voxel colors represent the values of the relative permittivity.

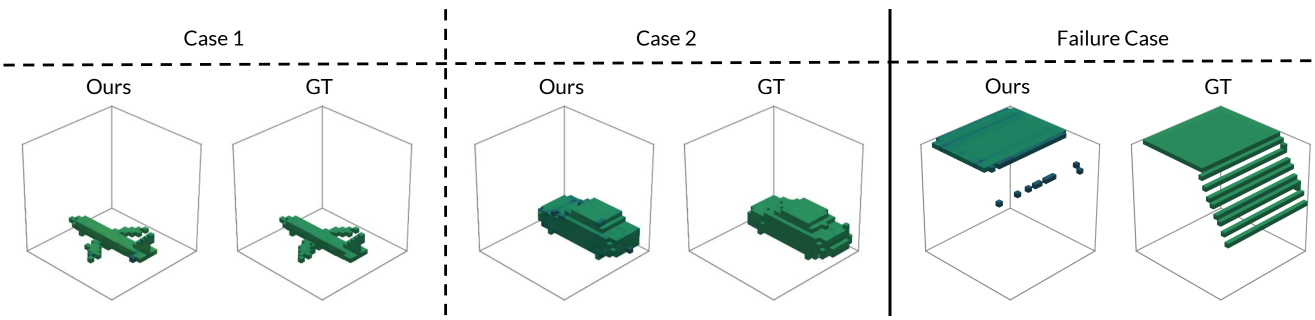

Figure 9. **Qualitative comparison under the single-transmitter setting for 3D reconstruction on 3D ShapeNet dataset.** The results are obtained with a single transmitter ($N = 1$). The voxel colors represent the values of the relative permittivity.

Fig. 1 provides a comprehensive comparison of reconstruction quality and runtime between the two methods for both $N = 1$ and $N = 6$ configurations. Fig. 8 and Fig. 9 provide visual comparisons of additional 3D reconstruction results on the 3D MNIST and 3D ShapeNet datasets. These results show that our method maintains robustness and generalizes effectively across geometrically complex 3D structures, representing significant progress towards practical applications.

6. Conclusion

In this work, we propose a fully end-to-end data-driven framework for electromagnetic inverse scattering that directly predicts relative permittivity from scattered field measurements. By leveraging data distribution priors to compensate for the lack of physical information, our method demonstrates state-of-the-art reconstruction accuracy and robustness, particularly in challenging single-transmitter scenarios where existing methods fail. This work highlights the potential of data-driven approaches to overcome the ill-posedness of inverse problems and provides a practical path toward cost-effective electromagnetic imaging.

Limitations. While our method effectively handles sparse transmitter settings, it struggles to reconstruct thin structures (see the rightmost block in Fig. 9 for a typical failure case) and cannot accommodate varying receiver or transmitter locations. These limitations challenge deployment in real-world scenarios, where sensor layouts and environmental complexity vary. Addressing fine-structure reconstruction and flexible sensor configurations remains an important direction for future work.

Acknowledgments

This work was supported by NSFC-6247070125, Ningbo Grants 2025Z038 and 2025Z059, and the High Performance Computing Center at Eastern Institute of Technology and Ningbo Institute of Digital Twin.

References

[1] Laura Anitori, Matern Otten, and Peter Hoogeboom. Compressive sensing for high resolution radar imaging. In *2010 Asia-Pacific Microwave Conference*, pages 1809–1812, 2010. 2

[2] Nicola Anselmi, Lorenzo Poli, Giacomo Oliveri, and Andrea Massa. Iterative multiresolution Bayesian CS for microwave imaging. *IEEE Trans. Antennas Propag.*, 66(7):3665–3677, 2018. 2

[3] Richard Baraniuk and Philippe Steeghs. Compressive radar imaging. In *2007 IEEE Radar Conference*, pages 128–133, 2007. 2

[4] Kamal Belkebir, Patrick C Chaumet, and Anne Sentenac. Superresolution in total internal reflection tomography. *Journal of the Optical Society of America A*, 2005. 2, 3, 5, 6, 14

[5] Martina Teresa Bevacqua, Simona Di Meo, Lorenzo Crocco, Tommaso Isernia, and Marco Pasian. Millimeter-waves breast cancer imaging via inverse scattering techniques. *IEEE Journal of Electromagnetics, RF and Microwaves in Medicine and Biology*, 5:246–253, 2021. 2

[6] Xudong Chen. Subspace-based optimization method for solving inverse-scattering problems. *IEEE Transactions on Geoscience and Remote Sensing*, 2009. 2, 5, 6, 14

[7] Xudong Chen. *Computational methods for electromagnetic inverse scattering*. John Wiley & Sons, 2018. 2, 5, 6, 12, 14

[8] David Colton and Rainer Kress. *Integral Equation Methods in Scattering Theory*. SIAM, 2013. 3, 11

[9] David L Colton, Rainer Kress, and Rainer Kress. *Inverse Acoustic and Electromagnetic Scattering Theory*. Springer, 1998. 12

[10] Giannis Daras, Hyungjin Chung, Chieh-Hsin Lai, Yuki Mitsufuji, Jong Chul Ye, Peyman Milanfar, Alexandros G. Dimakis, and Mauricio Delbracio. A survey on diffusion models for inverse problems, 2024. 2

[11] David de la Iglesia Castro. 3D mnist: A 3D version of the mnist database of handwritten digits. https://www.kaggle.com/datasets/daavoo/3d-mnist. 5, 7, 12, 14

[12] Li Deng. The mnist database of handwritten digit images for machine learning research. *IEEE Signal Processing Magazine*, 29(6):141–142, 2012. 5, 11, 13, 14

[13] AJ Devaney. Inverse-scattering theory within the rytov approximation. *Optics Letters*, 1981. 2

[14] Fuqiang Gao, Barry D Van Veen, and Susan C Hagness. Sensitivity of the distorted born iterative method to the initial guess in microwave breast imaging. *IEEE Transactions on Antennas and Propagation*, 2015. 2

[15] Jean-Michel Geffrin, Pierre Sabouroux, and Christelle Eyraud. Free space experimental scattering database continuation: experimental set-up and measurement precision. *Inverse Problems*, 21(6):S117–S130, 2005. 5, 6, 12

[16] Ruixu Geng, Yang Hu, Yan Chen, et al. Recent advances on non-line-of-sight imaging: Conventional physical models, deep learning, and new scenes. *APSIPA Transactions on Signal and Information Processing*, 2021. 3

[17] Ruixu Geng, Yadong Li, Dongheng Zhang, Jincheng Wu, Yating Gao, Yang Hu, and Yan Chen. Dream-pcd: Deep reconstruction and enhancement of mmwave radar pointcloud. *IEEE Transactions on Image Processing*, 2024. 1

[18] Tarek M Habashy, Ross W Groom, and Brian R Spies. Beyond the born and rytov approximations: A nonlinear approach to electromagnetic scattering. *Journal of Geophysical Research: Solid Earth*, 1993. 2

[19] Tarek M Habashy, Michael L Oristaglio, and Adrianus T de Hoop. Simultaneous nonlinear reconstruction of two-dimensional permittivity and conductivity. *Radio Science*, 1994. 2

[20] Melvin Johnson, Mike Schuster, Quoc V. Le, Maxim Krikun, Yonghui Wu, Zhifeng Chen, Nikhil Thorat, Fernanda Viégas, Martin Wattenberg, Greg Corrado, Macduff Hughes, and Jeffrey Dean. Google's multilingual neural machine translation system: Enabling zero-shot translation, 2017. 14

[21] Ulugbek Kamilov, Charles Bouman, Gregery Buzzard, and Brendt Wohlberg. Plug-and-play methods for integrating physical and learned models in computational imaging: Theory, algorithms, and applications. *IEEE Signal Processing Magazine*, 40:85–97, 2023. 2

[22] Michael Leigsnering, Christian Debes, and Abdelhak M. Zoubir. Compressive sensing in through-the-wall radar imaging. *IEEE*, 2011. 2

[23] Lianlin Li, Long Gang Wang, Fernando L. Teixeira, Che Liu, Arye Nehorai, and Tie Jun Cui. Deepnis: Deep neural network for nonlinear electromagnetic inverse scattering. *IEEE Transactions on Antennas and Propagation*, 67(3):1819–1825, 2019. 2, 3

[24] Yadong Li, Dongheng Zhang, Ruixu Geng, Jincheng Wu, Yang Hu, Qibin Sun, and Yan Chen. Ifnet: Imaging and focusing network for handheld mmwave devices. In *IEEE International Conference on Acoustics, Speech and Signal Processing (ICASSP)*, 2024. 3

[25] Zicheng Liu, Dominique Lesselier, and Yu Zhong. Electromagnetic imaging of damages in fibered layered laminates via equivalence theory. *IEEE Trans. Comput. Imaging*, 4(2): 219–227, 2018. 2

[26] Zicheng Liu, Mayank Roy, Dilip K Prasad, and Krishna Agarwal. Physics-guided loss functions improve deep learning performance in inverse scattering. *IEEE Transactions on Computational Imaging*, 2022. 2, 3, 5, 6, 11, 13, 14

[27] Ziyuan Luo, Boxin Shi, Haoliang Li, and Renjie Wan. Imaging interiors: An implicit solution to electromagnetic inverse scattering problems. In *ECCV*, 2024. 1, 2, 3, 5, 6, 7, 11, 13, 14

[28] Sanjit K Mitra. *Digital signal processing: a computer-based approach*. McGraw-Hill Higher Education, 2001. 11

[29] Natalia K. Nikolova. Microwave imaging for breast cancer. *IEEE Microwave Magazine*, 12(7):78–94, 2011. 2

[30] Giacomo Oliveri, Marco Salucci, Nicola Anselmi, and Andrea Massa. Compressive sensing as applied to inverse problems for imaging: Theory, applications, current trends, and open challenges. *IEEE Antennas Propag. Mag.*, 59(5):34–46, 2017. 2

[31] Declan O'Loughlin, Martin O'Halloran, Brian M Moloney, Martin Glavin, Edward Jones, and M Adnan Elahi. Microwave breast imaging: Clinical advances and remaining challenges. *IEEE Transactions on Biomedical Engineering*, 65(11):2580–2590, 2018. 1, 2

[32] Li Pan, Yu Zhong, Xudong Chen, and Swee Ping Yeo. Subspace-based optimization method for inverse scattering problems utilizing phaseless data. *IEEE Transactions on Geoscience and Remote Sensing*, 49(3):981–987, 2011. 2

[33] Andrew F Peterson, Scott L Ray, and Raj Mittra. *Computational methods for electromagnetics*. IEEE Press New York, 1998. 3, 11, 12

[34] Leonid Rudin, Stanley Osher, and Emad Fatemi. Nonlinear total variation based noise removal algorithms. *Physica D: Nonlinear Phenomena*, 60:259–268, 1992. 14

[35] Yash Sanghvi, Yaswanth Kalepu, and Uday K Khankhoje. Embedding deep learning in inverse scattering problems. *IEEE Transactions on Computational Imaging*, 2019. 3, 5

[36] Fangfang Shen, Guanghui Zhao, Zicheng Liu, Guangming Shi, and Jie Lin. SAR imaging with structural sparse representation. *IEEE J. Sel. Topics Appl. Earth Observ. Remote Sens.*, 8(8):3902–3910, 2014. 2

[37] M. Slaney, A.C. Kak, and L.E. Larsen. Limitations of imaging with first-order diffraction tomography. *IEEE Transactions on Microwave Theory and Techniques*, 1984. 2

[38] Lin-Ping Song, Chun Yu, and Qing Huo Liu. Through-wall imaging (twi) by radar: 2-d tomographic results and analyses. *IEEE Trans. Geosci. Remote. Sens.*, 43:2793–2798, 2005. 2

[39] Rencheng Song, Youyou Huang, Kuiwen Xu, Xiuzhu Ye, Chang Li, and Xun Chen. Electromagnetic inverse scattering with perceptual generative adversarial networks. *IEEE Transactions on Computational Imaging*, 2021. 2, 3, 5, 6, 7, 11, 13, 14

[40] Allen Taflove, Susan C Hagness, and Melinda Piket-May. Computational electromagnetics: the finite-difference time-domain method. *The Electrical Engineering Handbook*, 2005. 11

[41] Peter M van den Berg, AL Van Broekhoven, and Aria Abubakar. Extended contrast source inversion. *Inverse problems*, 1999. 2

[42] Ji-Yuan Wang and Xiao-Min Pan. Universal approximation theorem and deep learning for the solution of frequency-domain electromagnetic scattering problems. *IEEE Transactions on Antennas and Propagation*, 72(12):9274–9285, 2024. 2

[43] Zhou Wang and Alan C. Bovik. Mean squared error: Love it or leave it? a new look at signal fidelity measures. *IEEE Signal Processing Magazine*, 26(1):98–117, 2009. 5, 13

[44] Zhou Wang, A.C. Bovik, H.R. Sheikh, and E.P. Simoncelli. Image quality assessment: from error visibility to structural similarity. *IEEE TIP*, 13(4):600–612, 2004. 5, 13

[45] Zhun Wei and Xudong Chen. Deep-learning schemes for full-wave nonlinear inverse scattering problems. *IEEE Transactions on Geoscience and Remote Sensing*, 57(4):1849–1860, 2019. 3, 5, 6, 11

[46] Zhirong Wu, Shuran Song, Aditya Khosla, Fisher Yu, Linguang Zhang, Xiaoou Tang, and Jianxiong Xiao. 3d shapenets: A deep representation for volumetric shapes. In *Proceedings of the IEEE conference on computer vision and pattern recognition*, pages 1912–1920, 2015. 5, 7, 12, 14

[47] Kuiwen Xu, Yu Zhong, and Gaofeng Wang. A hybrid regularization technique for solving highly nonlinear inverse scattering problems. *IEEE Transactions on Microwave Theory and Techniques*, 2017. 2

[48] Kuiwen Xu, Chen Zhang, Xiuzhu Ye, and Rencheng Song. Fast full-wave electromagnetic inverse scattering based on scalable cascaded convolutional neural networks. *IEEE Transactions on Geoscience and Remote Sensing*, 2021. 3

[49] Haining Yang, Tingjun Li, Na Li, Zhiming He, and Qing Huo Liu. Efficient near-field imaging for single-borehole radar with widely separated transceivers. *IEEE Transactions on Geoscience and Remote Sensing*, 53(10):5327–5337, 2015. 2

[50] He Ming Yao, Wei E. I. Sha, and Lijun Jiang. Two-step enhanced deep learning approach for electromagnetic inverse scattering problems. *IEEE Antennas and Wireless Propagation Letters*, 18(11):2254–2258, 2019. 2, 5

[51] He Ming Yao, Lijun Jiang, and Wei E. I. Sha. Enhanced deep learning approach based on the deep convolutional encoder–decoder architecture for electromagnetic inverse scattering problems. *IEEE Antennas and Wireless Propagation Letters*, 19(7):1211–1215, 2020.

[52] Xinling Yu, José E. C. Serrallés, Ilias I. Giannakopoulos, Ziyue Liu, Luca Daniel, Riccardo Lattanzi, and Zheng Zhang. Pifon-ept: Mr-based electrical property tomography using physics-informed fourier networks. *IEEE Journal on Multiscale and Multiphysics Computational Techniques*, 9:49–60, 2024. 2

[53] Lu Zhang, Kuiwen Xu, Rencheng Song, Xiuzhu Ye, Gaofeng Wang, and Xudong Chen. Learning-based quantitative microwave imaging with a hybrid input scheme. *IEEE Sensors Journal*, 2020. 3

[54] Yu Zhong and Xudong Chen. Twofold subspace-based optimization method for solving inverse scattering problems. *Inverse Problems*, 2009. 2, 5

[55] Yu Zhong and Xudong Chen. An fft twofold subspace-based optimization method for solving electromagnetic inverse scattering problems. *IEEE Transactions on Antennas and Propagation*, 2011. 2

[56] Yu Zhong, Marc Lambert, Dominique Lesselier, and Xudong Chen. A new integral equation method to solve highly nonlinear inverse scattering problems. *IEEE Transactions on Antennas and Propagation*, 64(5):1788–1799, 2016. 2

[57] Huilin Zhou, Yang Cheng, Huimin Zheng, Qiegen Liu, and Yuhao Wang. Deep unfolding contrast source inversion for strong scatterers via generative adversarial mechanism. *IEEE Transactions on Microwave Theory and Techniques*, 2022. 11, 12